Performance and implementation of centrifugal serpentine micromixers with non-rectangular cross-section

Joshua A Clark[1]**, Tahir A Butt**[1]**, Gautam Mahajan**[2]**,**
Chandrasekhar R Kothapalli[2]🔘**, Miron Kaufman**[1] **and Petru S Fodor**[1]🔘

[1] Department of Physics, Cleveland State University, Cleveland, OH, United States of America
[2] Department of Chemical and Biomedical Engineering, Cleveland State University, Cleveland, OH, United States of America

E-mail: p.fodor@csuohio.edu

CrossMark

Abstract

The fluid flow and mixing characteristics of planar serpentine microchannels consisting of repeating S-shaped units was characterized both computationally and experimentally for Reynolds numbers Re < 100. In particular, it was found that using non-rectangular cross-sections with changing orientation for the geometrical units greatly enhances their mixing performance relative to standard rectangular profile serpentine channels. The optimization of the cross-section enables efficient mixing of two-fluid components at Reynolds numbers as low as 20, making these designs practical for chemical reaction engineering and biological assays platforms. A computational analysis of the cross-sectional flow structures present in this type of channels indicates that their enhanced performance is correlated with the formation of secondary transversal vortexes. In the optimal designs, their presence increases the mass transfer in the microchannel by both stretching the interface between the fluid components to be mixed, as well as by promoting chaotic advection.

Keywords: micromixers, dean flows, serpentine microchannels, mixing optimization, chaotic advection

(Some figures may appear in colour only in the online journal)

1. Introduction

Microfluidic platforms have been widely regarded as defining technologies for the development of chemical and biological synthesis and analysis systems [1, 2]. The benefits of miniaturizing these processes include, reduced reactant consumption [3], increases by orders of magnitude of the surface-to-volume ratios [4], greatly enhanced control over reaction's variables such as temperature and pressure [1, 5], and more straightforward scalability from laboratory prototype reactors to large-scale production through device parallelization and numbering up [6, 7]. These have made them viable candidates for applications ranging from the production of nanoparticles [8], to the synthesis of colloidal systems [9] and monodisperse droplets [10] that require stringent control of the final product composition and size.

However, it has to be noted that one of the bottlenecks for their wider adoption in reaction engineering platforms are the challenges encountered in promoting efficient mixing in micro-scale flows. At the flow rates practically achievable in devices fabricated through popular and cost-efficient prototyping methodologies [11], the fluid flow is laminar and the primary mechanism for mixing different chemical and biological species relies on molecular diffusion [12–14]. Unfortunately, this can be too slow for systems where fast reaction kinetics competes with diffusion-driven mass transfer, leading to the formation of depletion zones and inefficient use of reagents [15–17].

Thus, in the context of microfluidics studies and applications, a broader effort has been dedicated to research on strategies targeted at enhancing mixing on these scales. Broadly, the methodologies employed seek to reduce the average distance over which the diffusion has to act to homogenize the system, either by splitting and folding fluid elements (lamination), or by promoting transversal flows that can both stretch the interface between the solutions to be mixed, as well as promote chaotic advection [11–13]. For the later strategy, achieving the necessary cross-sectional stretching and folding of the fluid elements has been realized through both active and passive mixing methodologies. Active mixers employ external energy sources to control the fluid flow. Designs based on ultrasonic vibration [18], artificial cilia structures [19], mechanical actuators [20], electrically driven flows [21], or magneto-hydrodynamic particles [11], have shown very good mixing capabilities. However, this comes at the expense of more complex architectures that have to combine both fluid flow and external control structures on the same chip, making scaling-up the number of devices from prototype versions challenging [22]. Moreover, in chemical reactions systems where maintaining isothermal conditions is critical, strategies that require for example electric control signals could further increase the complexity of the designs to provide the necessary heat management [23]. On the other hand, passive micromixers rely only on the existing pressure differential required to push the fluids of interest along the microfluidic system, using strategically designed geometrical features placed in the path of the fluid flow to induce stirring flows [24]. These include ridge-groove systems on the channel walls [25–27], obstacles [28, 29] or barriers [30], and various curved or angled turns [31–36]. While the mixing quality can be smaller than that achievable in active devices, their fabrication is amenable to a variety of techniques including soft-lithography [37, 38], 3D printing [39], and molecular imprinting [40]. Additionally, since one does not have to account for the complex physics interactions present in actively controlled devices, but only for the fluid dynamics and the concentration-diffusion of the different species, computational fluid dynamics (CFD) has proved to be very successful in allowing the modeling of this type of mixers [17, 26, 38]. This has provided a powerful tool for efficiently testing new designs and identifying their optimal parameters.

One of the simplest and first methodologies used in passive micromixers designs to geometrically induce transversal stirring employed microchannel systems with curved sections [12]. Forcing the fluids to move along curved geometries induces transversal vortices, also known as Dean flows, that can be used to promote cross-sectional advective mixing. Aside from using easy to fabricate topologies such as planar spirals and serpentines, this particular approach also presents useful characteristics for applications when compared with other more complex geometries used in passive micromixers such as ridge/groove systems or obstacles. They are easy to flush out after use and thus can be re-usable [41]. Also, the peak shear rates in these types of devices are small making them attractive for biological applications where large biomolecules and particles have to be handled without damage

[42, 43]. Their major disadvantage though is that the reliance on centrifugal forces for their functioning requires large fluid speeds (Re > 100) for efficient mixing [12, 44, 45]. While transversal flows are present at any fluid speed, in the low Reynolds number regime, they are symmetric with the fluid components mostly confined in distinct regions of the microchannel. In typical serpentine channels, only for Re > 100, the symmetry is broken and flow bifurcations occur leading to enhanced mixing through chaotic advection [12]. However, due to the large pressure differentials needed the corresponding flow rates are challenging to achieve in many of their potential applications. While modifications added to the walls of the channels, such as flow directing grooves [46], sinusoidal modulations of their surfaces [47], the use of 3D turns as part of the mixing units [48], employing triangular cross-sections [49, 50], or using non-aligned inlets [51] have improved their performance as a function of Reynolds number, they have come at the expense of more complex fabrication and have diminished their potential advantages relative to other micromixers designs.

An alternative approach to control the symmetry and distribution of the transversal Dean flows is the use of non-rectangular cross-sections for the mixing units [52]. In this work, we combine this with changes in the cross-section orientation between the serpentine segments to break the symmetry of the flows and induce secondary vortexes. The designs proposed and investigated show enhanced mixing capabilities compared with standard serpentine mixers, while preserving the simple planar designs of the channels and without requiring obstructions placed in the path of the flow. CFD and particle tracing simulations are used to analyze how the transversal flow structure changes as a function of the geometrical parameters, and associate the increase in the mixing performance observed with the onset of chaotic advection. Prototypes of the designs proposed have also been experimentally tested to both validate the numerical work and illustrate the increased performance of these micromixers when compared with standard serpentine micromixers with rectangular cross-section.

2. Mixer design

The basic topologies the mixers investigated are shown in figures 1 and 2. The fluid components are introduced through separate inlets into a main channel of width W and height H.

In both the types of designs explored, each mixing unit is S-shaped, with two semicircular sections with an inner radius R_{in} connected by a short straight section with length equal with W (see *xy* projection of mixing unit in figure 1). For the standard (i.e. rectangular cross-section) serpentine micromixer (figure 1), the cross-sections of the mixing units were identical to that of the main channels connecting the inlets and outlet to the mixing section.

On the other hand, for the proposed modified design in the mixing unit, the cross-section of the channel has a non-rectangular step shape with the size of the step being given by h_{step} and w_{step} in z and y axes, respectively (figure 2). Between each half mixing cycle, the orientation of the cross-section
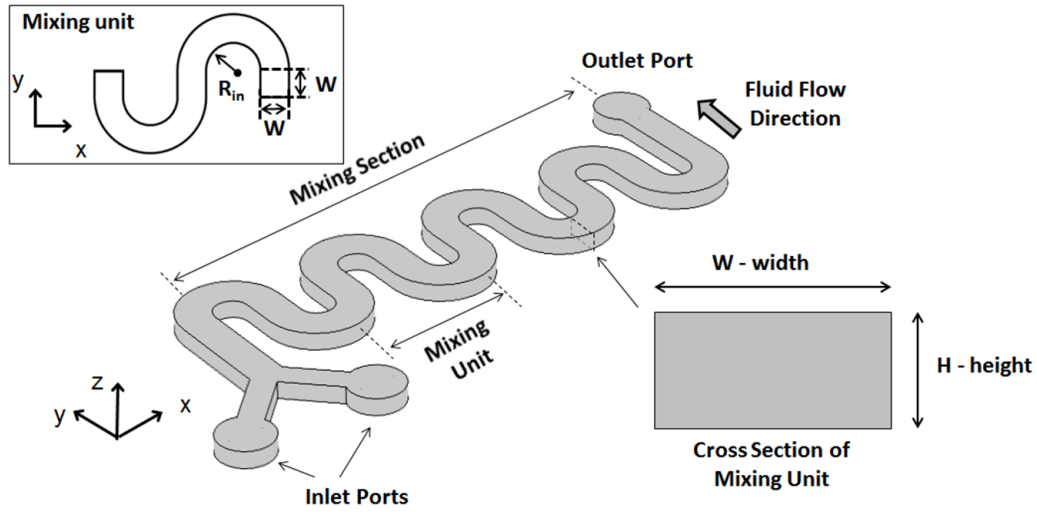
Figure 1. Topology of standard (rectangular cross-section) serpentine micromixers. In actual experimental implementations of the designs, the number of mixing units in the mixing section could be larger than that shown in this figure, as required to achieve full mixing before the outlet.
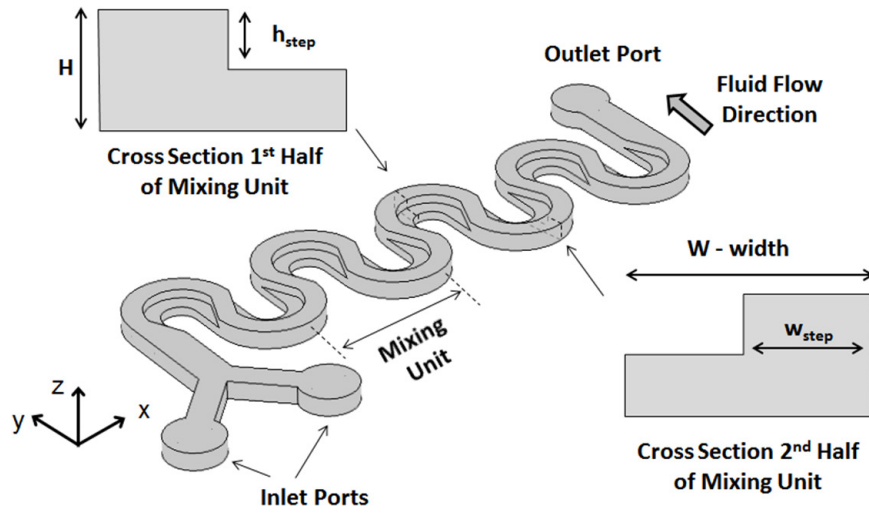

Figure 2. Topology of modified serpentine mixer in which a non-rectangular cross-section for the mixing unit was used. As described in the text, the orientation of the section changes halfway through each mixing unit.

was changed, so that the thicker part of the step cross-section is always on the outside part of the mixing unit.

3. Numerical and experimental implementation

3.1. Numerical methods

To determine the flow fields for all the geometries investigated, the governing equations for momentum and mass conservation, i.e. the Navier–Stokes equations of motion and the continuity equation for an incompressible Newtonian fluid, were solved numerically:

$$\rho \left[\frac{\partial \boldsymbol{u}}{\partial t} + (\boldsymbol{u} \cdot \nabla) \boldsymbol{u} \right] = -\nabla p + \eta \nabla^2 \boldsymbol{u} \tag{1}$$

$$\nabla \cdot \mathbf{u} = 0 \tag{2}$$

where u [m/s] is the velocity vector, ρ [kg/m^3] is the fluid density, η [kg/(m $\cdot$ s)] is the fluid viscosity, t [s] is the time, and

p [Pa] is the pressure. The basic settings for the numerical problem are: pressure driven flow with zero pressure at the outlet and steady flow rates at the inlets, and no-slip boundary conditions for all the walls. The flow-field simulations were performed using the computational package COMSOL Multiphysics 5.3a (COMSOL Inc., Stockholm Sweden) and its CFD/Chemical Engineering Modules. The solutions were obtained using a generalized minimal residual method (GMRES) iterative solver with a geometrical multigrid pre-conditioner and a Vanka algorithm for the pre- and post-smoothing. The geometry was discretized using tetrahedral mesh elements with typical element sizes of $W/40$, resulting in a number of mesh elements of no less than 750 000 for all the simulations.

Subsequently, the concentration distributions of distinct species to be mixed in the micromixers were determined by numerically solving the concentration-diffusion equation in the same computational package:

$$\frac{\partial c}{\partial t} = D\nabla^2 c - \boldsymbol{u} \cdot \nabla c \qquad (3)$$

where c [mol/m^3] is the concentration of the species of interest and D [m^2/s] is its diffusion constant, respectively. To avoid the typical numerical errors associated with modeling mass transport phenomena [53], the concentration-diffusion equation was solved by mapping the velocity field obtained from the Navier–Stokes equation, onto a much finer tetrahedral mesh with typical element sizes of $W/70$ resulting in no less than 3 500 000 elements for all the simulations. The accuracy of the numerical models employed has been validated against a broad range of passive microfluidic mixers employing geometrical features to induce transversal flow [38, 54]. Specifically, when compared with experimental results on planar curved microchannels, both in this work and for related studies [55], we found our computational model to be in agreement with the experimental results in terms of both the concentration distribution maps as well as mixing measures such as the mixing time.

Aside from mapping the concentration distributions, point massless particle tracers were also used to obtain insights into the advection inside the microchannels, decoupled from the diffusional component. To achieve this, a Lagrangian particle tracing method was employed in which the equation of motion for particles released at the inlets was solved:

$$\frac{d\overrightarrow{r_i}}{dt} = \vec{u}(\overrightarrow{r_i}) \qquad (4)$$

where $\overrightarrow{r_i}$ is the position of each individual particle i, and $\vec{u}(\overrightarrow{r_i})$ is the velocity at the position of each particle location obtained from the fluid velocity field given by the Navier–Stokes equations [27].

3.2. Device prototyping and characterization

Prototypes of the proposed designs and of the standard serpentine microchannels have been fabricated using established methodologies for fabricating microfluidic devices using soft-lithography [37, 38]. In brief, positive relief structures with the desired channel dimensions were fabricated on silicon wafers using two-layer photolithography, at the California NanoSystems Institute, University of California at Santa Barbara facilities, based on our SolidWorks® designs. Subsequently, replicas of the channels were produced by pouring PDMS (polydimethylsiloxane, Sylgard 184; Dow Corning) over the silicon molds and curing it. To complete the devices, the resulting replicas of the channels were plasma-treated and bounded/sealed to glass slides. The fluids to be mixed were fed into the inlet ports from 10 ml syringes, attached to the ports of the devices with 1/16″ inner diameter tubing (Clearflex 60) and 90° elbow joints (McMasterCarr). A similar tubing set-up was used to discharge the effluent fluid at the outlet. To obtain the necessary steady flow rates, the syringes were loaded in calibrated syringe pumps (e.g. Harvard Instruments PicoPlus).

The prototypes were first tested under a low-magnification wide-field microscope using green and blue food dyes, to check for the overall performance and leaks. Subsequently, a Nikon A1 Rsi confocal microcopy system was used to obtain high-resolution images of the species distribution in the mixer. To this end, fluorescent dye solutions (10 μM) of 10 kDa FITC-dextran and 10 kDa rhodamine B-dextran, respectively, were pumped into the separate inlets, at equal flow rates. The distribution of the two dyes along the mixer was imaged in the xy plane (parallel with the direction of the flow) using a $10\times$ objective lens. In order to map the distribution of the dyes in the volume of the mixer, up to 200 slices in the z-direction (perpendicular to the flow direction) were taken. Since each xy slice acquired covers about the length of one mixing unit, overlapping xy acquisitions at the same z position were stitched together to map the dye distribution along mixing sections formed by multiple mixing units. The image processing was done using the NIH ImageJ (version 1.51j8) package as well as the Nikon NIS-Elements C control software.

4. Results and discussion

Representative numerical results for the modeling of the flow field and concentration distribution in the two types of micromixers were shown in figure 3. For all the simulations and the experimental implementations in this work, the width and height of the main channel were set to $W = 200$ μm and $H = 100$ μm, consistent with the typical dimensions used in previous studies of serpentine micromixers [49, 50, 54]. The inner radius of the curved sections of the mixing units was set to $R_{in} = W/2 = 100$ μm. The average flow speeds at the entrance of the mixing section were varied from 0.075 m s^{-1} to 0.75 m s^{-1}, corresponding to Reynolds numbers from 10 to 100. The two components to be mixed were introduced in the system on opposite halves of the inlet using step-like concentration profiles. The diffusion constant D was set to 1.0×10^{-9} m^2 s^{-1}, which is the corresponding diffusion range for most ions in aqueous solutions. To streamline the optimization process, the modeling was done for a mixing section composed of only two mixing units. While such a geometrical unit is too short to achieve full mixing by its outlet, it does allow for the mixing dependence on the geometrical parameters to be computationally characterized efficiently.

As observed from the evolution of the cross-sectional concentration maps along the channel (figure 3), for both types of mixers, transversal flows develop due to the centrifugal forces experienced by the fluids as they are forced to move along curved trajectories. This induced circulation is apparent in the redistribution across the cross-section of the channel of the chemical species introduced on different sides of the inlet, as the fluid moves along the channel. In the first approximation, the presence of these cross-sectional flows leads to a stretching of the interface between the regions occupied by the two components, which in turn is expected to be beneficial to the ability of the molecular diffusion to mix them. However, it has to be noted, that for the rectangular cross-section mixers, in the low Reynolds number regime, i.e. Re < 100, the associated increase in the mixing quality is limited and confined to a narrow boundary, as the two components while moving
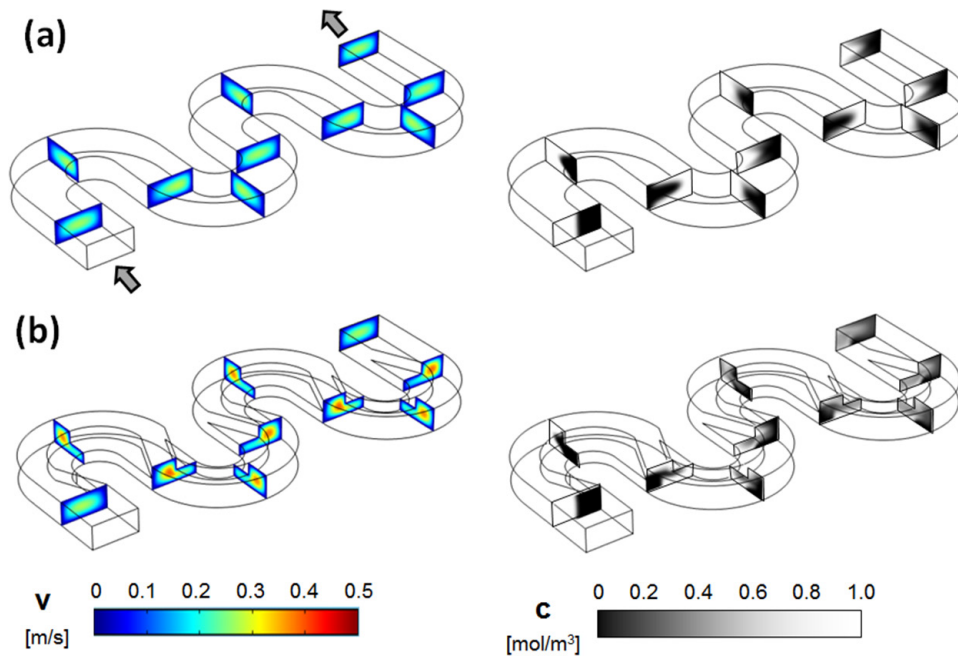
Figure 3. Flow fields and concentration distributions in (a) rectangular, and (b) non-rectangular cross-sections, respectively, of the serpentine micromixer (Re = 20).
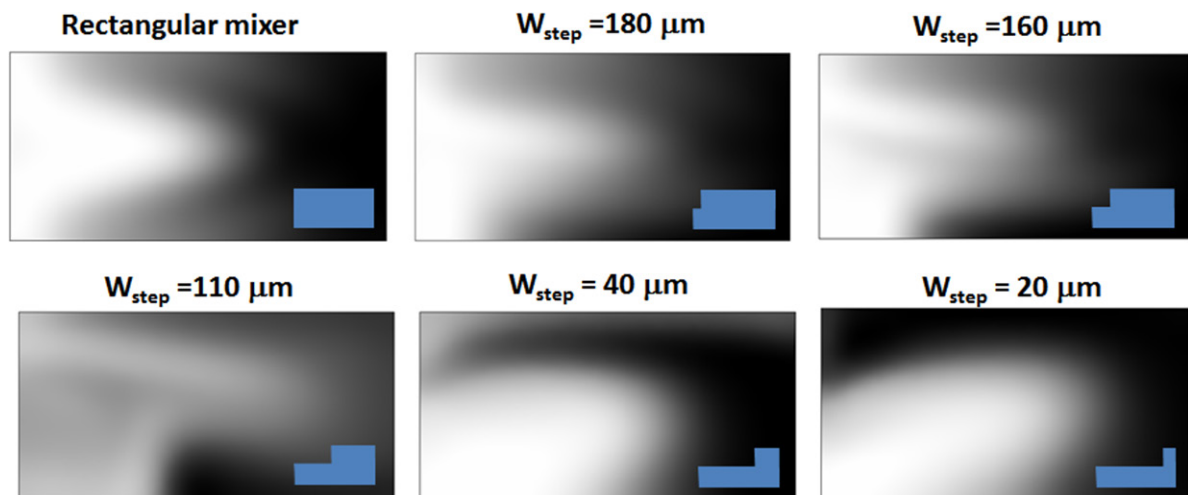

Figure 4. Concentration distributions at the outlet of serpentine micromixers with different cross-sections, after two complete mixing units. The insets show a cross-sectional of the channel profile within the mixing unit (Re = 20, h_{step} = 50 μm, for all the results shown).

along helical trajectories remain largely confined into distinct regions even after two mixing units.

On the other hand, cross-sectional concentration profiles for non-rectangular cross-section mixers showed a more complex behavior. As illustrated in figure 4, for Re = 20, as the cross-section of the mixing unit was changed from a rectangular shape to a non-rectangular step-like shape defined by different values chosen for w_{step}, qualitatively much more uniform concentration distributions could be achieved. Specifically, for microchannels with w_{step} in the range 160 μm to 40 μm, the effect of the stretching of the interface between the components to be mixed appears to be supplemented by lamination. For these particular designs, the concentration maps show the appearance of filament-like structures that break the continuity of the regions containing a single chemical component. At

low Reynolds numbers, similar structures have been observed in other types of efficient passive micromixers, such as the staggered herring bone type mixers [25], where they resulted in both enhanced contact area between the components to be mixed, as well as chaotic advection. Previous studies on Dean flow micromixers have observed these types of effects but only at Reynolds numbers at least an order of magnitude higher [12], which require the corresponding devices to sustain very large pressure drops. While an increase in the pressure drop is present in the non-rectangular cross-section channels described here due to the decreased cross-section, this increase is only by a factor of about ~2 relative to their rectangular cross-section counterparts for Re = 20 and w_{step} = 110 μm. In this context, the above data indicates that the use of non-rectangular cross-sections for the mixing units
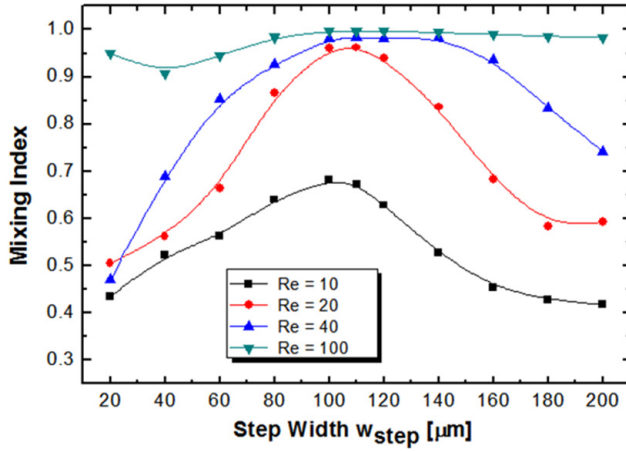
Figure 5. Mixing index dependence on the geometrical parameter w_{step} and the Reynolds number ($h_{step} = 50$ μm).

is a viable strategy to improve their mixing performance and more importantly to reduce the flow rates required to values that can be handled through standard microfluidics fabrication methodologies.

While the visual analysis of the concentration distribution images at the outlet provides a qualitative assessment of the various mixers performance, a more rigorous mixing measure is needed in order to identify the optimal geometrical parameters defining their cross-section and operation range. To this end, the concentration images of the different chemical components at the outlet, such as those shown in figure 4, were processed as 8-bit grayscale intensity maps divided into a number (N_{bins}) of equal size regions (also referred as bins). Subsequently, as detailed in [55], for a system with two components, the level of homogeneity can be assessed by calculating the global Shannon entropy associated with the map as:

$$M = -\frac{1}{\ln 2} \cdot \frac{1}{N_{bins}} \cdot \sum_{j=1}^{N_{bins}} \left[p_{1/j} \ln \left(p_{1/j} \right) + p_{2/j} \ln \left(p_{2/j} \right) \right] \quad (5)$$

where M is referred to as a mixing index, and $p_{1/j}$ and $p_{2/j}$, with $p_{1/j} + p_{2/j} = 1$, are probabilities for components 1 and 2, respectively, conditional on being located in bin j. They represent the fraction of components 1 and 2, respectively, in each bin relative to the total and are calculated as the ratio of the average bin intensity normalized by the maximum intensity, i.e. 255 for grayscale image data. As shown in equation (5), the mixing index M is normalized by a factor of $\ln(2)$ (where 2 corresponds to the number of components) fixing its range of values from $M = 0$ (corresponding to completely segregated components) to $M = 1$ (corresponding to maximum global homogeneity, i.e. perfect mixing). Aside from being mathematically rigorous and easy to interpret, this mixing index is easily applicable to a broad range of both simulation and experimental data that encode the quantity of interest in image intensities [55].

Figure 5 summarizes the mixing performance of a broad set of designs with w_{step} in the range 20 μm to 200 μm, with $h_{step} = 50$ μm. The range of Reynolds numbers explored was from 10 to 100. For all the designs, the performance is

strongly dependent on the Reynolds number, with better mixing being achieved at higher Reynolds numbers. This can be understood in terms of increased strength of the centrifugal forces experienced by the fluids as the flow rates are increased, and the fact that these forces are the primary drivers for the transversal flows present in these channels. In fact, in the large Reynolds number regime, i.e. Re $\geqslant$ 100, the performance of all the designs was quite good, approaching the optimal value $M = 1$, consistent with previous observations that typical Dean type micromixers require operation at large flow rates to be efficient [12]. As the Reynolds number is decreased though, the evolution in the performance of the different micromixers is very distinct. For designs with small or large w_{step}, i.e. corresponding to sections that are close to rectangular ones, the mixing efficiency expectedly deteriorates rapidly with decreased Reynolds number. On the other hand, in agreement with the qualitative assessment from concentration maps, for designs with w_{step} in the range 100 μm to 120 μm and $h_{step} \sim 50$ μm, the mixing performance holds well, down to Re = 20.

While the performance of the proposed mixers remains close to the optimal point (~1) for Reynolds numbers Re = 20, they show superior mixing abilities even for Reynolds numbers as low as 10, when compared with standard serpentine micromixers. To gain insights into the flow field topologies present in these devices and responsible for the advection of the chemical components, streamline plots were reconstructed from the solutions to the Navier–Stokes equations (figure 6).

As expected for the rectangular type mixer, the cross-sectional streamline plots mapped after the first mixing unit showed the formation of two symmetric counter-rotating Dean vortices, that are the drivers of the transversal flows in these devices. However, as the cross-section is modified to a step-like one, the map becomes more complicated with the symmetry of the vortices being broken by the constraints of the non-rectangular cross-section. This leads to changes in the center of rotation of the cross-sectional vortices between the mixing units, and thus to elongational flows. More importantly, for the mixer designs that have been found superior based on their mixing performance (i.e. with $w_{step} = 100$–120 μm), the formation of a well-defined third vortex is noticeable in the cross-section (figure 6; $w_{step} = 110$ μm). These types of secondary flows that both break the reflection symmetry of the flow pattern, as well as lead to extensive stretching and folding of the fluid elements have been observed in other performant mixers based on curved mixing sections [12, 54, 56, 57]. However, in all those cases, the transition to this flow regime occurred at flow rates and Reynolds numbers at least an order of magnitude larger, making the current strategy to control the flow topology at low Reynolds numbers particularly effective.

The transition from a flow structure characterized by symmetric cross-sectional flows, to one dominated by secondary flows and the development of additional vortices, is associated with a progression from a mixing mechanism dominated by the increased contact area between the components to be mixed, to one dominated by chaotic advection [12]. In the designs studied here, this was apparent in the evolution of the interface between the two components. This can be explored
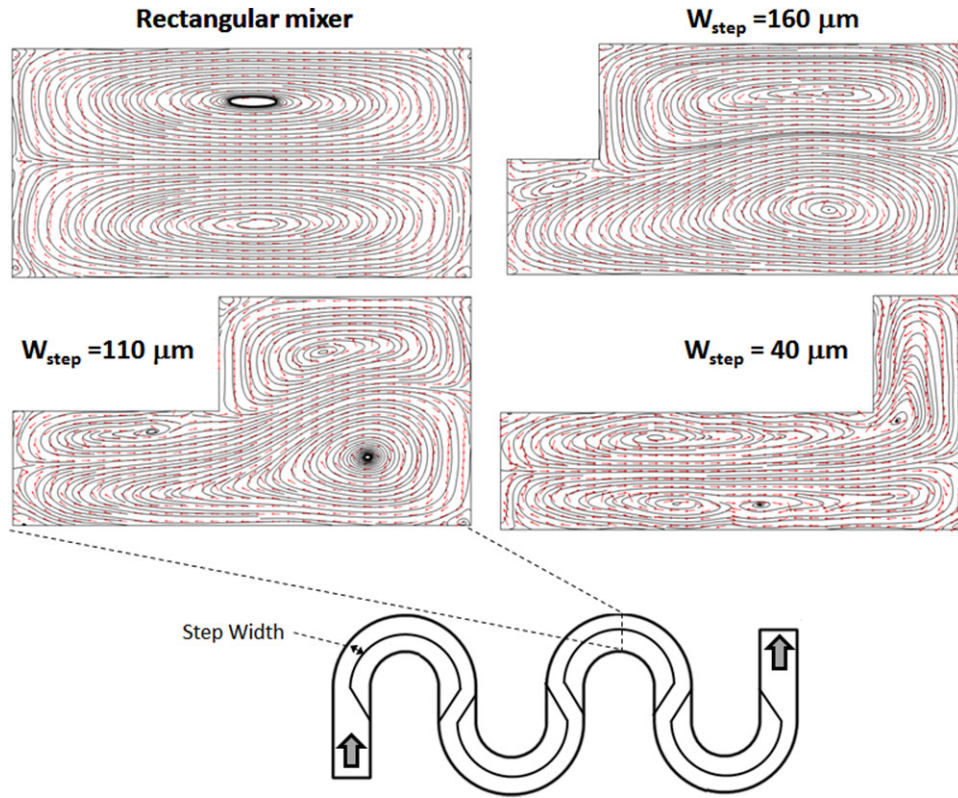
Figure 6. Cross-sectional streamline plots of the velocity field for mixers with different cross-sections. The velocity field is mapped after the first mixing unit (Re = 20).

computationally using particle tracing. In our study, a thousand massless point particles were being released at the inlet of the mixing unit, equally spaced along the line defining the interface between the components to be mixed. Their time evolution, as they are advected by the flow in the micromixers, was then monitored. Figure 7 shows both their trajectories as well as Poincaré maps of their distribution at the outlet of the channels. In all the geometries explored, stretching of the initial interface between the two components was present, as indicated by the lateral motion of the particles as they are driven through the channel. For the rectangular cross-section mixer, the Poincaré maps are reflection symmetric with respect to the longitudinal dissecting plane of the channels, reflecting the symmetry of the counter-rotating transversal flows present.

As the cross-section is changed to a non-rectangular shape, two effects are observed. First, sections of the initial interface suffer enhanced stretching and also their symmetry is broken. This is a directed consequence of the non-symmetric flow topology. The increased contact area between the components correlates with slightly increased mixing relative with the rectangular channel design. Second, as the cross-section reaches geometrical parameters in the range $w_{step} = 100–120$ μm (figure 7(c)), the connectedness of the particles initially on the interface line quickly deteriorates, and particles that initially were in close proximity are now being spread far apart from each other across the transversal section of the channel.

This loss of correlation between the nearest particles is a strong indicator that for these particular designs, the flow transitions into a much more complex behaviour, akin to

chaotic advection. In this respect, it is then not surprising that the mixing quality for this particular set of mixers is greatly improved relative to their counterparts. A qualitative measure of the correlation between each particle and its initial neighbours can be achieved by calculating the time evolution of the average Euclidean distance between the nearest neighbours:

$$\Delta r(t) = \frac{1}{N_p - 1} \sum_{k=1}^{N_p - 1} |\vec{r}_{t,\,k+1} - \vec{r}_{t,\,k}| \qquad (6)$$

where N_p is the number of particles in the chain, and $\vec{r}_{t,\,k+1}$ and $\vec{r}_{t,\,k}$ are the time-dependent position vectors of the particles $k + 1$ and k, respectively, in the chain. Time evolutions of these averages for different designs are shown in figure 8. For all studies, the average distance between particles at the interface is expected to increase, both due to the longitudinal advection, as the particles near the walls move slower, as well as due to the cross-sectional flows present in all these devices. However, as the symmetry of the interface is broken, the rate at which the particles move away from each other increases, with the slope of this rise being maximum for designs with $w_{step} \sim 110$ μm. Moreover, in these particular designs, the slope of the increase changes dramatically during the second part of the first mixing cycle, signaling a rapid deterioration of the correlation between the particles, and the possible onset of chaotic advection as the fluid is stretched and folded between the mixing units. While the mixing sections modeled were too short to be able to calculate the Lyapunov exponents associated with the divergence of the particle trajectories, the divergence of the Euclidean distance is an indicator that the Lyapunov
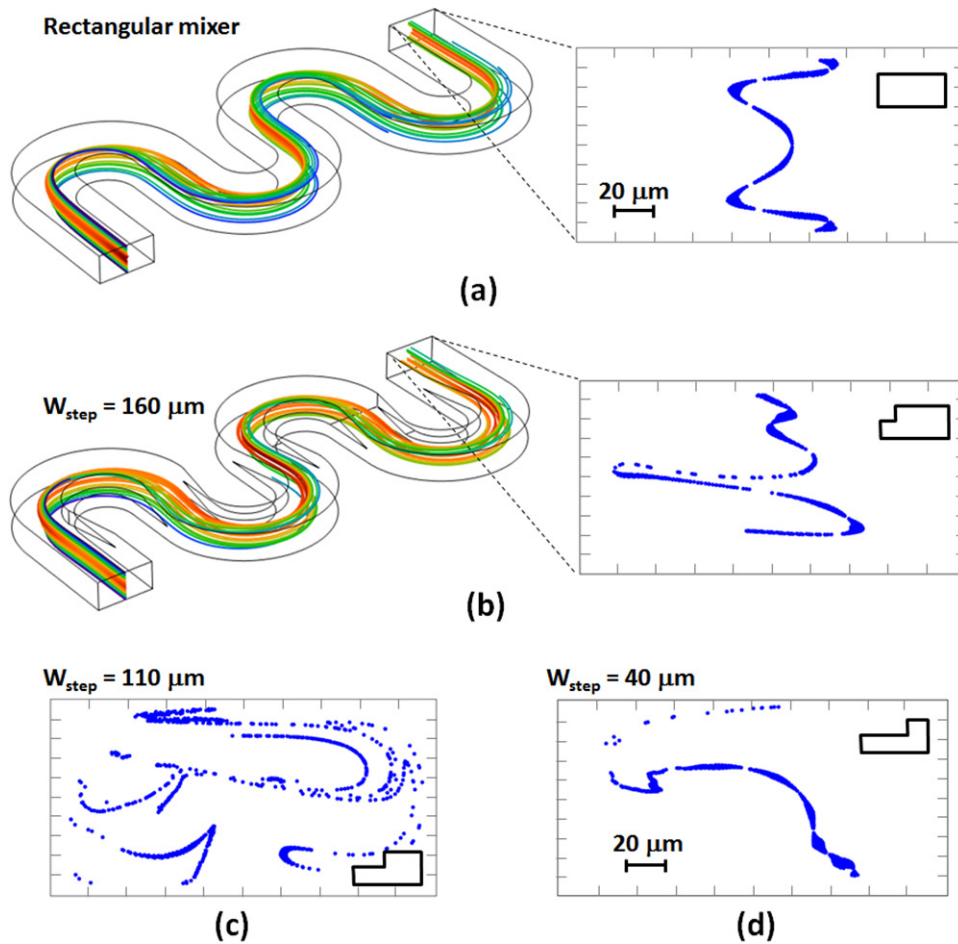
Figure 7. Particle tracing and Poincaré map of the particles at the outlet for (a) rectangular mixer, and (b) non-rectangular mixer with $w_{step} = 160$ μm. Poincaré maps of the particles at the outlet for mixers with (c) $w_{step} = 110$ μm, and (d) $w_{step} = 40$ μm (Re = 20). The initial release point of the particles is along the interface between the two components.
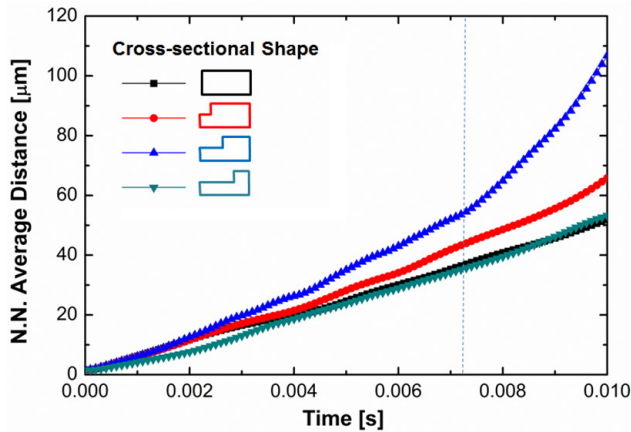

Figure 8. Temporal evolution of the average distance between the nearest neighbors for designs with varying cross-sections, from rectangular cross-section to a w_{step} of 160 μm, 110 μm, and 40 μm (Re = 20). The vertical dotted line indicates the residence time necessary for an average particle to pass over the first half of the first mixing unit.

exponents for such a system assume positive values, signaling chaotic flows [58]. As the w_{step} of the designs is decreased further (e.g. $w_{step} = 40$ μm), the increase in the average Euclidean distance settles back to a slower rise, similar with that of the

rectangular cross-section channel. This is also associated with a recovery in the cohesiveness of the interface between the components (figure 7(d)), as well as the rapid decrease in the mixing quality achievable. Nevertheless, this result is consistent with the fact that as the cross-section parameter w_{step} is made smaller, the transversal section of the channel converges back to a rectangular shape, albeit with a larger aspect ratio. Thus, the flow structure returns to the topology consisting of two symmetric counter-rotating vortexes.

As discussed in section 3.2, although slightly more complex, the non-rectangular cross-section designs investigated were easily fabricated using popular microfluidic device prototyping methods based on replica-molding and soft-lithography. For comparison purposes, micromixers based on the optimized design as well as their standard rectangular cross-section counterparts were fabricated. The dimensions used for the main channel were the same as in the computational study, i.e. $W = 200$ μm and $H = 100$ μm. In the experimental implementation, each mixing section consisted of five mixing units.

Evolution of the dye distributions along the channels investigated show consistency with the computational investigation. At low Reynolds numbers, in the standard rectangular cross-section micromixer, even if cross-sectional movement
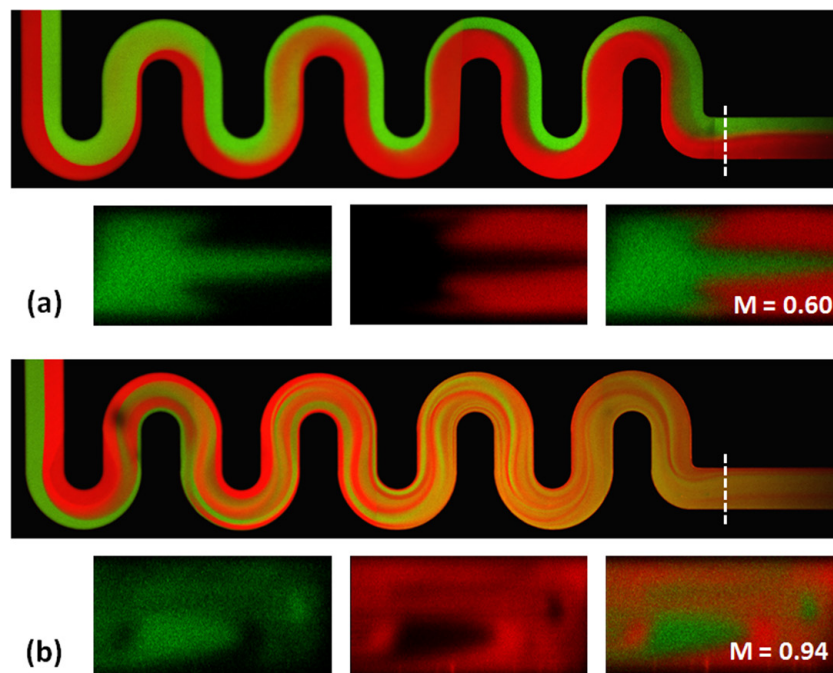
Figure 9. Confocal microscopy images of fluorescence FITC-dextran (green) and rhodamine B-dextran (red) streams in (a) a standard rectangular cross-section planar serpentine mixer ($W = 200$ μm and $H = 100$ μm); and (b) an optimized non-rectangular cross-section mixer ($w_{step} = 110$ μm and $h_{step} = 50$ μm). In each set, the bottom images correspond to the cross-sectional distribution of the FITC-dextran (green), the rhodamine B-dextran (red), and the composite distribution, respectively, at the outlet in the *y-z* plane (the dotted line indicates the position of the section) for Re = 20.

due to the Dean's flow is present, the two dyes introduced on separate sides of the inlet remain largely separated. Even after five mixing units, the regions occupied by the different components are distinct, with the cross-talk confined in the narrow region of contact between them. In contrast, for the non-rectangular cross-section design, rapid lamination of the two components occur, in as early as the first mixing unit. This is rapidly compounded by the subsequent mixing units. Cross-sectional images of each dye distribution at the outlet confirm this conclusion (figure 9). While for the standard serpentine mixer, the interface between the two components is stretched, there are large areas in the cross-section that contain only one species. In the new topology designs, the individual dye distribution at the outlet is more uniform with each component being much better distributed across the whole cross-section. Quantitative assessment of the mixing quality, based on the same methodology used for the computational optimization, provides mixing indexes of $M = 0.60$ for the rectangular cross-section channels, versus $M = 0.94$ for the new designs. These are in agreement with the mixing indexes determined from numerical implementations of the same structures, which were $M = 0.64$ and $M = 0.98$ respectively, with the new designs showing consistently much better performance at Reynolds numbers Re < 100.

5. Conclusions

Numerical simulations and experimental studies have been used to show that the use of non-rectangular cross-section in serpentine Dean flow micromixers is a viable strategy to

enhance their mixing performance at low Reynolds numbers. Optimized designs exhibit quick lamination after the first mixing unit driven by the onset of chaotic advection. Numerical investigations of the flow field structure indicate that this is correlated with the symmetry breaking associated with the non-symmetric cross-section and the development of secondary vortices. The transition is akin with that observed in the popular staggered herringbone topology versus the slated groove topology, where the symmetry breakage and the axial movement of the center of rotation of the cross-sectional flows, subjects the fluid flow to repeated rotational and extensional flows [25]. In previous implementations of Dean flow micromixers, transitioning to this regime was possible only at very large flow rates and pressure drops. In this context, the topology studied and proposed provides a practical methodology to design highly efficient serpentine microreactors accessible to standard microfluidic fabrication methods. Moreover, the high mixing quality in these designs was achieved without using complex geometrical obstructions and flow-controlling features that are both prone to clogging, as well as difficult to flush out.

Acknowledgments

ORCID iDs

Chandrasekhar R Kothapalli (ORCID) https://orcid.org/0000-0001-8450-0640
Petru S Fodor (ORCID) https://orcid.org/0000-0003-0936-5316

References

[1] Geong G S, Chung S and Kim C B 2010 Applications of micromixing technology *Analyst* **135** 460–73
[2] Chiu D T, deMello A J, Di Carlo D, Doyle P S, Hansen C, Maceiczyk R M and Wootton R C R 2017 Small but perfectly formed? Successes, challenges, and opportunities for microfluidics in the chemical and biological sciences *Chem* **2** 201–23
[3] Makgwane P R and Ray S S 2014 Synthesis of nanomaterials by continuous-flow microfluidics: a review *J. Nanosci. Nanotechnol.* **14** 1338–63
[4] Ehrfeld W, Hessel V and Lowe H 2004 *Microreactors: New Technology for Modern Chemistry* (Weinheim: Wiley)
[5] Günther A and Jensen K F 2006 Multiphase microfluidics: from flow characteristics to chemical and materials synthesis *Lab Chip* **6** 1487–503
[6] Hessel V, Kralisch D and Krtschil U 2008 Sustainability through green processing—novel process windows intensify micro and milli process technologies *Energy Environ. Sci.* **1** 467–78
[7] Roberge D M, Gottsponer M, Eyholzer M and Kockmann N 2009 Industrial design, scale-up, and use of microreactors *Chim. Oggi* **27** 8–11
[8] Zhao C X, He L, Qiao S Z and Middleberg A P J 2011 Nanoparticle synthesis in microreactors *Chem. Eng. Sci.* **66** 1463–79
[9] Khan S A, Günther A, Schmidt M A and Jensen K F 2004 Microfluidic synthesis of colloidal silica *Langmuir* **20** 8604–11
[10] Li W, Young E, Seo M, Nie Z, Garstecki P, Simmons C and Kumacheva E 2008 Simultaneous generation of droplets with different dimensions in parallel integrated microfluidic droplet generators *Soft Matter* **4** 258–62
[11] Nguyen N-T and Wu Z 2005 Mixers—a review *J. Micromech. Microeng.* **15** R1
[12] Nguyen N-T 2012 *Micromixers: Fundamentals, Design and Fabrication* 2nd edn (Oxford: Elsevier)
[13] Lee C Y, Chang C L, Wang Y N and Fu L M 2011 Microfluidic mixing: a review *Int. J. Mol. Sci.* **12** 3263–87
[14] Rismanian M, Saidi M S and Kashaninejad N 2019 A new non-dimensional parameter to obtain the minimum mixing length in tree-like concentration gradient generators *Chem. Eng. Sci.* **195** 120
[15] D'Alessandro J and Fodor P S 2014 Improving fuel consumption in microfluidic based fuel cells *Fuel Cells* **14** 818
[16] Mouza A, Patsa C-M and Schönfeld F 2008 Mixing performance of a chaotic micro-mixer *Chem. Eng. Res. Des.* **86** 1128–34
[17] Hermann P, Timmermann J, Hoffmann M, Schlüter M, Hofmann C, Löb P and Ziegenbalg D 2018 Optimization of a split and recombine micromixer by improved exploitation of secondary flows *Chem. Eng. J.* **334** 1996–2003

[18] Brandhoff L, Zirath H, Salas M, Haller A, Peham J, Wiesinger-Mayr H, Spittler A, Schnetz G, Lang W and Vellekoop M J 2015 A multi-purpose ultrasonic streaming mixer for integrated magnetic bead ELISAs *J. Micromech. Microeng.* **25** 104001
[19] Toonder J D *et al* 2008 Artificial cilia for active micro-fluidic mixing *Lab Chip* **8** 533–41
[20] Abbas Y, Miwa J, Zengerle R and von Stetten F 2013 Active continuous-flow micromixer using an external braille pin actuator array *Micromachines* **4** 80–9
[21] Krishnaveni T, Renganathan T, Picardo J R and Pushpavanam S 2017 Numerical study of enhanced mixing in pressure-driven flows in microchannels using a spatially periodic electric field *Phys. Rev.* E **96** 033117
[22] Capretto L, Cheng W, Hill M and Xhang X 2011 Micromixing within microfluidic devices *Top. Curr. Chem.* **304** 27–68
[23] Miralles V, Huerre A, Malloggi F and Jullien M-C 2013 A review of heating and temperature control in microfluidic systems: techniques and applications *Diagnostics* **3** 33–67
[24] Hessel V, Löwe H and Schönfeld F 2005 Micromixers—a review on passive and active mixing principles *Chem. Eng. Sci.* **60** 2479–501
[25] Stroock A D, Dertinger S K W, Ajdari A, Mezic I, Stone H A and Whitesides G M 2002 Chaotic mixer for microchannels *Science* **295** 647–51
[26] Kee S P and Gavriilidis A 2008 Design and characterization of the staggered herringbone mixer *Chem. Eng. J.* **142** 109–21
[27] Fodor P S F and Kaufman M 2011 The evolution of mixing in the staggered herring bone micromixer *Mod. Phys. Lett.* B **25** 1111–25
[28] Kim D S, Lee S W, Kwon T H and Lee S S 2004 A barrier embedded chaotic micromixer *J. Micromech. Microeng.* **15** 798–805
[29] Chen L, Wang G, Lim C, Seong G H, Choo J, Lee E K, Kang S H and Song J M 2009 Evaluation of passive mixing behaviors in a pillar obstruction poly(dimethylsiloxane) microfluidic mixer using fluorescence microscopy *Microfluid. Nanofluid.* **7** 267
[30] Alam A, Afzal A and Kim K-Y 2014 Mixing performance of a planar micromixer with circular obstructions in a curved microchannel *Chem. Eng. Res. Des.* **92** 423–34
[31] Scherr T, Quitadamo C, Tesvich P, Park D S, Tiersch T, Hayes D, Choi J W, Nandakumar K and Monroe W T 2012 A planar microfluidic mixer based on logarithmic spirals *J. Micromech. Microeng.* **22** 055019
[32] Chen X and Li T 2016 A novel design for passive micromixers based on topology optimization method *Biomed. Microdevices* **18** 57
[33] Qi N, Li B, You H, Zhang W, Fu L, Wang Y and Chen L 2014 Surface-enhanced Raman scattering on a zigzag microfluidic chip: towards high-sensitivity detection of As(III) ions *Anal. Methods* **6** 4077
[34] Chen X and Zhang S 2018 A novel macromodel based on Krylov subspace projection method for micromixers with serpentine channels *Int. J. Nonlinear Sci. Numer. Simul.* **19** 275
[35] Raza W, Hossain S and Kim K-Y 2018 Effective mixing in a short serpentine split-and-recombination micromixer *Sens. Actuators* B **258** 381
[36] Su B, Meng J, Zhang Z, Liu F and Zhang A 2015 Fabrication of alumina micromixer with two-dimensional serpentine microchannels by centrifuge-assisted micromoulding *Micro Nano Lett.* **10** 703
[37] Tsao C-W 2016 Polymer microfluidics: simple, low-cost fabrication process bridging academic lab research to commercialized production *Micromachines* **7** 225
[38] Hama B, Mahajan G, Fodor P S, Kaufman M and Kothapalli C R 2018 Evolution of mixing in a microfluidic

reverse-staggered herringbone micromixer *Microfluid. Nanofluid.* **22** 54

[39] Waheed S, Cabot J M, Macdonald N P, Lewis T, Guijt R M, Paullab B and Breadmore M C 2016 3D printed microfluidic devices: enablers and barriers *Lab Chip* **11** 1993–2013

[40] Sun G, Panpan W, Shenguang G, Lei G, Jinghua Y and Mei Y 2014 Photoelectrochemical sensor for pentachlorophenol on microfluidic paper-based analytical devicebased on the molecular imprinting technique *Biosens. Bioelectron.* **56** 97–103

[41] Araci I E, Robles M and Quake S R 2016 A reusable microfluidic device provides continuous measurement capability and improves the detection limit of digital biology *Lab Chip* **16** 1573–8

[42] Liu R H, Stremler M A, Sharp K V, Olsen M G, Santiago J G, Adrian R J, Aref H and Beebe D J 2000 Passive mixing in a three-dimensional serpentine microchannel *J. Microelectromech. Syst.* **9** 190–7

[43] Nivedita N and Papautsky I 2013 Continuous separation of blood cells in spiral microfluidic devices *Biomicrofluidics* **7** 054101

[44] Mengeaud V, Josserand J and Girasult H H 2002 Mixing processes in a zigzag microchannel: finite element simulation and optical study *Anal. Chem.* **74** 4279–86

[45] Chen X, Li T, Zeng H, Hu Z and Fu B 2016 Numerical and experimental investigation on micromixers with serpentine microchannels *Int. J. Heat Mass Transfer* **98** 131–40

[46] Cook K J, Fan Y and Hassan I 2013 Mixing evaluation of a passive scaled-up serpentine micromixer with slanted grooves *J. Fluids. Eng.* **135** 081102

[47] Javaid M U, Cheema T A and Park C W 2018 Analysis of passive mixing in a serpentine microchannel with sinusoidal side walls *Micromachines* **9** 8

[48] Sayah A and Gijs M A M 2016 Understanding the mixing process in 3D microfluidic nozzle/diffuser systems: simulations and experiments *J. Micromech. Microeng.* **26** 115017

[49] Shamloo A, Madadelahi M and Akbari A 2016 Numerical simulation of centrifugal serpentine micromixers and analyzing mixing parameters *Chem. Eng. Process.* **104** 243–52

[50] Filimonov R and Sorvari J 2017 Numerical study on the effect of cross-section orientation on fluid flow and heat transfer in a periodic serpentine triangular microchannel *Appl. Therm. Eng.* **125** 366–76

[51] Hossain S and Kim K-Y 2015 Mixing performance of a serpentine micromixer with non-aligned inputs *Micromachines* **6** 842–54

[52] Clark J, Kaufman M and Fodor P S 2018 Mixing enhancement in serpentine micromixers with non-rectangular cross-section *Micromachines* **9** 107

[53] Kuzmin D 2010 *A Guide to Numerical Methods for Transport Equations* (Erlangen: Friedrich-Alexander-Universität Erlangen-Nürnberg)

[54] Jiang F, Drese K S, Hardt S, Küpper M and Schönfeld F 2004 Helical flows and chaotic mixing in curved micro channels *AIChE J.* **50** 2297–305

[55] Camesasca M, Manas-Zloczower I and Kaufman M 2005 Entropic characterization of mixing in microchannels *J. Micromech. Microeng.* **15** 2038–45

[56] Aref H 1984 Stirring by chaotic advection *J. Fluid. Mech.* **143** 1

[57] Fodor P S, Vyhnalek B and Kaufman M 2013 Entropic evaluation of Dean flow micromixers *Proc. of the 2013 COMSOL Conf. (Boston, MA)* pp 9–11

[58] Wolf A, Swift J B, Swinney H L and Vasato J A 1985 Determining Lyapunov exponents from a time series *Physica* D **16** 285–317